POLITECNICO DI TORINO
Repository ISTITUZIONALE

An investigation on the effect of powder recycling on the microstructure and mechanical properties of AISI 316L produced by Directed Energy Deposition

Original
An investigation on the effect of powder recycling on the microstructure and mechanical properties of AISI 316L produced by Directed Energy Deposition / Saboori, A., Aversa, A., Bosio, F., Bassini, E., Librera, E., De Chirico, M., Biamino, S., Ugues, D., Fino, P., Lombardi, M.. - In: MATERIALS SCIENCE AND ENGINEERING A-STRUCTURAL MATERIALS PROPERTIES MICROSTRUCTURE AND PROCESSING. - ISSN 0921-5093. - ELETTRONICO. - 766:(2019). [10.1016/j.msea.2019.138360]

Availability:
This version is available at: 11583/2749868 since: 2023-08-24T08:15:39Z

Publisher:
Elsevier

Published
DOI:10.1016/j.msea.2019.138360

Terms of use:

This article is made available under terms and conditions as specified in the corresponding bibliographic description in the repository

Publisher copyright

(Article begins on next page)

19 November 2026

Materials Science & Engineering A 766 (2019) 138360

Contents lists available at ScienceDirect

Materials Science & Engineering A

journal homepage: www.elsevier.com/locate/msea

An investigation on the effect of powder recycling on the microstructure and mechanical properties of AISI 316L produced by Directed Energy Deposition

Abdollah Saboori[a,*], Alberta Aversa[a], Federico Bosio[a], Emilio Bassini[a], Erica Librera[b], Michele De Chirico[b], Sara Biamino[a], Daniele Ugues[a], Paolo Fino[a], Mariangela Lombardi[a]

[a] Department of Applied Science and Technology, Politecnico Di Torino, Corso Duca degli Abruzzi 24, 10129, Torino, Italy
[b] Prima Industries SpA, Via Trino Pianezza36, 10093, Collegno To, Italy

ARTICLE INFO

Keywords:
Additive manufacturing
Directed energy deposition
AISI 316L
Microstructure
Mechanical properties

ABSTRACT

Directed energy deposition (DED) has been employed to produce AISI 316L samples. Microstructure and primary cellular arm spacing (PCAS) are studied analysing the relationship with the cooling rate at the different heights of DED processed 316L stainless steel sample. It is found that, by increasing the deposition distance from the substrate, the PCAS of the sample increases from 2.9 to 4.5 μm, as a consequence of the decreased cooling rate and thermal gradient. On the other hand, in the last deposited layers, the PCAS of the sample decreases from 4.5 to 3.3 μm, because of the changes in cooling mechanisms. The phase composition of samples after deposition is revealed and compared with the predictions based on the Schaeffler and Pseudo-binary diagrams. It is revealed that the final microstructure is characterized by austenitic dendrites together with some residual delta ferrite located at dendritic arms location. Lastly, the effect of using fresh or recycled powders, on the microstructure and mechanical properties of DED 316L stainless steel parts is investigated. It is found that the samples fabricated using recycled powders have rather similar tensile strength levels, but much lower elongation than those produced using fresh powder due to a lower inclusions content and of their average lower size. The nature of these inclusions is discussed as well as the reason for their increase both in numbers and size.

1. Introduction

Laser Additive Manufacturing (LAM) includes a set of processes in which three-dimensional metallic components can be produced in a layerwise fashion using the heating provided by a laser source [1]. Among LAM techniques, Directed Energy Deposition (DED) is one of the primary LAM technologies in the production of complex shaped parts with a high strength-to-weight ratio and minimum material wastage [2,3]. For this reason, in recent years, DED has been widely employed in the aerospace, petrochemical, automotive and power generation sectors [4,5]. In the DED process, the powder is blown atop the surface of a building substrate by single or multiple nozzles within an inert atmosphere. The energy provided by a high powered laser beam allows immediately the melting of powder, which is injected into the molten pool. Starting with a CAD solid model and using a sliced. STL file format, deposited parts are formed layer-upon-layer from bottom to top [6].

Fully built parts can be produced by using the optimum process parameters such as laser power, scanning speed, laser focus, hatching distance and z-step parameter [7]. The main interactions among the used process parameters lead to a complicated thermal history, which affects the incident energy and the melt pool geometry. As a consequence of this complex thermal history, various microstructures and mechanical properties can be achieved. For instance, high local energy and high scanning speed result in a large thermal gradient and high cooling rates that generate complicated and strong hydrodynamic fluid flows. Consequently, these phenomena have a marked influence on crystal growth and orientation, material spattering and microstructural defects, such as pores and partially melted particles [8].

Austenitic stainless steels have been extensively processed by DED during the past two decades [9–11]. Actually, owing to the combination of relatively good mechanical properties and excellent corrosion resistance, AISI 316L has been widely used and studied [11,12]. First of all, this alloy presents good weldability and, as a consequence, processability characteristics mainly thanks to its low carbon content (< 0.03 wt%). On the other hand, since the machining of austenitic steels is rather expensive due to its adhesive behaviour, the DED technique is highly appealing since the production of complex steel components can be obtained in a single fabrication step, thus limiting the need for costly machining steps. Moreover, such a technique allows

* Corresponding author.
E-mail address: abdollah.saboori@polito.it (A. Saboori).

https://doi.org/10.1016/j.msea.2019.138360
Received 18 July 2019; Received in revised form 29 August 2019; Accepted 30 August 2019
Available online 03 September 2019
0921-5093/ © 2019 The Authors. Published by Elsevier B.V. This is an open access article under the CC BY license (http://creativecommons.org/licenses/BY/4.0/).

the achievement of near net shaped structures with limited overstock, thus enabling for expensive metals savings, such as in the case of Ni, Cr, and Mo. Furthermore, the insertion of joints or welds within the part design can be limited or completely avoided.

A considerable number of works from open literature has been focused on mechanical properties of AISI 316L parts produced by DED [13–16]. Regarding this, earlier investigators showed that the time interval between the deposition of consecutive layers has a significant effect on tensile behaviour [17]. In fact, they demonstrated that with higher time interval, the cooling rate increases and, accordingly, materials with finer microstructure, higher strength and lower elongation to failure are obtained. Furthermore, Ziętala et al. produced 316L samples by DED with anisotropic mechanical properties [16]. The lowest values of yield and ultimate tensile strengths (YS and UTS, respectively) were recorded in a perpendicular direction to the deposited layers, probably for the numerous processing pores at the interlayer boundaries. Other researchers analysed the influence of deposition strategies on mechanical properties of DED-316L specimens [14,18]. They found that tensile test samples prepared according to the weaving scanning path exhibit higher tensile properties [18]. Moreover, Ma et al. correlated the size of primary cellular arm spacing (PCAS) with YS, UTS and microhardness [2]. According to their study, by applying higher energy density, coarser PCASs are generated and, as a consequence, lower mechanical properties are obtained. Lately, Wang et al. observing the influences of a pulse laser on the characteristics of DED parts, stated that higher strengthened part was realized using low inputted energy as a consequence of a high cooling rate and very fine microstructure [19]. Nevertheless, neither of the referred studies considered powder recycling and its effect on the microstructure and mechanical properties of 316L DED samples. To date, this aspect remains unstudied and, from an industrial point of view, there would be an urgent need to explore the hypothesis of recycling powder to minimize material wastage. Hence, this study is aimed at better understanding the effect of the starting powder, i.e. as-received (fresh) or recycled, on the microstructure and mechanical behaviour of DED samples. Furthermore, a correlation between the deposition height, PCAS size and cooling rate and phase composition of specimens are investigated in detail.

2. Materials and methods

2.1. Materials

In this research, AISI 316L pre-alloyed, gas atomized powder with a particle size in the range of 50–150 μm was used (d_{10} = 63.3 μm, d_{50} = 85.4 μm, d_{90} = 135.2 μm). The chemical composition of as-received 316L powder, reported in Table 1, is in accordance with AISI 316L powder used in the previous works [12,20,21]. In this work, as-received powder and recycled powder, i.e. un-melted powder particles recovered by previous DED trials, were used as starting material.

Fig. 1(a and b) shows the morphology of the fresh and recycled AISI 316L powder. According to Fig. 1, both powders consist of mostly spherical particles. Roughly 50% of such spherical particles exhibit smooth surface, whereas the rest exhibit the satellites, that are typical defects of gas atomized powders. Further to spherical particles, few irregular elongated particles are present in the batch and, although this occurs in few cases, sometimes satellites are very pronounced. In addition to such common features, recycled AISI 316 powder (Fig. 1 (b)) shows the presence of splats (melted and irregularly re-solidified material adhering on other particles) and surface oxides (yellow arrows). Furthermore, cross-section analysis of both powders revealed that recycling of powder has no influence on the porosity, inclusion content and microstructure of powders (supplementary material 1). The Oxygen content of starting and recycled powders was analysed using the inert gas fusion method by a LECO ONH836 Oxygen/Nitrogen/Hydrogen elemental analyser. Carbon and sulfur levels were measured by infrared absorption carbon-sulfur analyzer (LECO CS844).

Table 1
The nominal chemical composition of AISI 316L stainless steel powder.

Composition	C	Si	Mn	Cr	Mo	Ni	Nb	Fe
Wt. %	0.02	0.5	1.8	16.7	2.0	10	0.02	Bal.

2.2. Experimental procedure

The production of rectangular 316L samples with a dimension of 20 × 20 × 10 mm was performed using the PRIMA prototyped DED system. A 3-axis CNC unit was used to control the movement of the X–Y deposition table and the Z axis. The machine is equipped with a Ytterbium laser generator (YLS 3000, IPG Laser) with power output between 0 and 3 kW. A commercial powder feeder was used to transfer powder to the deposition head, with four coaxial multi-nozzles (4-way) (Fig. 2). Nitrogen with 99.99% purity was used as the carrier gas. All the experiments were performed under protective shielding gas (N_2) with 99.99% purity. Austenitic stainless steel plates with 150 × 150 × 6 mm size were used as a substrate material for deposition. In order to control the contamination level during the deposition, every plate was cleaned and degreased with acetone before the process.

Fully dense 316L specimens were produced by using the optimized process parameters that were defined in previous work from the same authors [20]. A standard alternating X/Y raster scanning strategy was used for the deposition of specimens.

2.3. Microstructural and mechanical characterization

After the deposition, specimens for microstructural analysis, which were rectangular bars of 10 × 20 × 30 mm were removed from the building substrate and polished by standard metallographic technique to obtain a mirror-like surface. Then, polished surfaces were etched with a solution of 15 mL HCl +10 mL HNO_3 + 1 mL acetic acid. Etchant has been applied by immersion for 9 s. Microstructural observations were carried out on etched cross-sections using the optical microscope LEICA DMI 5000 M and the Merlin Zeiss Supra TM 40 field emission microscope (FESEM) equipped with an EDS analysis system. FESEM micrographs were acquired at different locations along the z-axis of deposition starting from the surface/substrate interface, i.e. at 1, 8, 14 and 18 mm from the building platform. Hence, to determine the cooling rate values, the PCAS parameter was measured at each location according to the method of the triangle proposed by Ma et al. [2]. As for the triangle method, three central points of any three adjacent cellular dendrites form a triangle. The average PCAS of the three cellulars is the average of three lengths of three sides of cellular dendrites. Each calculated PCAS value is obtained by averaging 40 measurements, and the average PCAS of the sample is the mean of all the measurements. Indeed, at each specific distance from the substrate (i.e. 2, 8, 14, 18 mm from the substrate) four images were acquired from the left to right side (along the x/y direction), and then on each image 10 measurements were implemented to include all the different PCAS sizes in the calculations.

The phase composition of specimens in the building direction, was analysed by X-ray diffraction (XRD) by using an X-Pert Philips diffractometer (Cu Kα) in a Bragg Brentano configuration in a 2θ from 30 to 100° (Operated at 40 kV and 40 mA with a step size 0.013 and 35 s per step). Moreover, the quantity of residual δ-ferrite is evaluated via image analysis method.

Tensile test samples were machined from 12 × 12 × 93 mm as-built bars obtained using both fresh and recycled powders in order to evaluate the effect of the starting raw material on mechanical properties. Two tensile samples perpendicular to the building direction, having dimensions complying with ASTM-E8 and 4 mm thickness, were

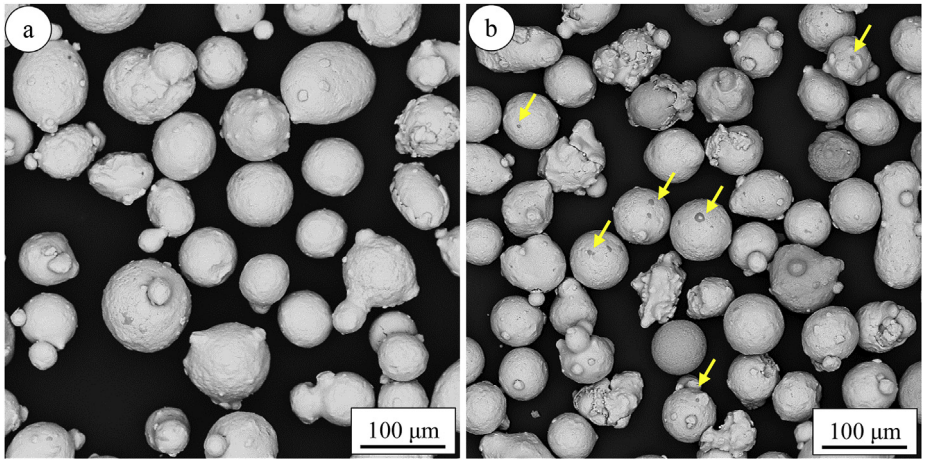


Fig. 1. SEM images of (a) fresh, and (b) recycled AISI 316L powder.

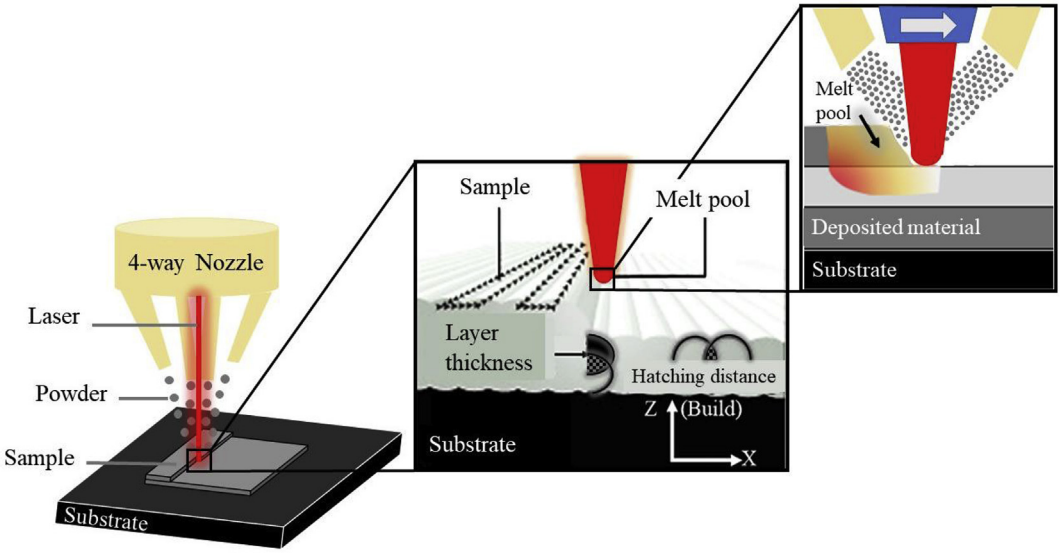


Fig. 2. Schematic of the deposition process and its process parameters.

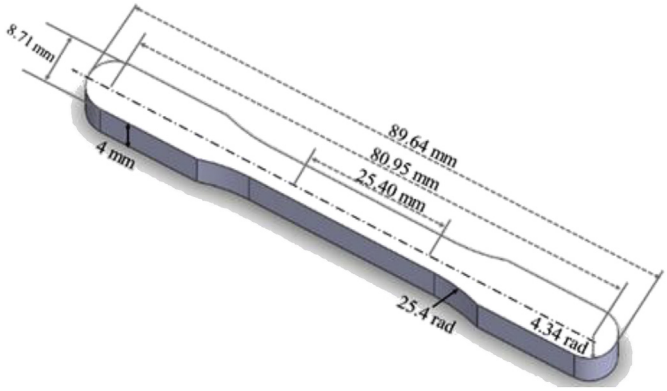


Fig. 3. Dimensional details of the flat specimen for tensile tests according to ASTM E8.

obtained from each bar (see Fig. 3). Four tensile measurements were performed through a Zwick Z100 testing system using $8 \times 10^{-3}\,s^{-1}$ as strain rate. Finally, a detailed investigation of fractured surfaces was carried out by means of FESEM. Moreover, the dynamic Young modulus value was evaluated by the impulse excitation technique by an IMCE RFDA basic instrument on $50 \times 20 \times 4$ mm samples machined from $54 \times 24 \times 12$ mm bars. Five measurements on each sample were carried out.

3. Results and discussion

3.1. Microstructure

Generally, in the DED process, the thermal history during part deposition plays a key role in the achievement of its specific microstructural features, like morphology and grain size. The resulting microstructure is mainly determined by the high heating/cooling rates, by marked temperature gradients, and by bulk temperature increments. Notwithstanding this, the prediction of the microstructural characteristics of a DED sample on the base of the many process variables/parameters involved is still an important challenge. Fundamentally, a microstructure is determined by a combination of factors like the temperature gradient (G), the travel speed of the solid/liquid interface (R), the undercooling and the alloy composition. In particular, the solidification morphology parameter (G/R) and the cooling rate levels ($G \times R$) define the solidification mode and therefore, the microstructure morphology and its inherent dimensions [22,23].

Despite some local differences along the sample, the rapid cooling rate in DED process, which could reach 10^3–10^4 K/s, contributes

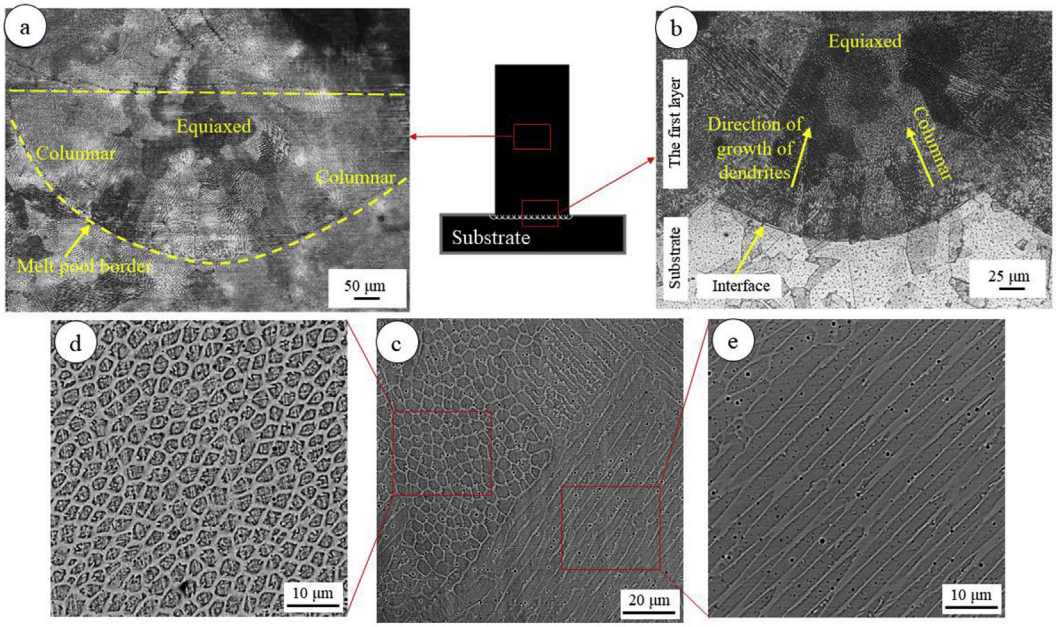


Fig. 4. Light optical microscopy micrographs of the DED AISI 316L steel samples produced using fresh powder: (a) a representative melt pool at the middle height, (b) the microstructure of the first layer, (c) SEM images the columnar and equiaxed microstructures refereeing to the last deposited layer, (d–e) high magnifications of (c)) from two different regions.

significantly to the refinement of the microstructure thus giving positive results in terms of mechanical properties.

In particular, the local variations in the G and R levels during deposition generate either columnar or equiaxed microstructures in stainless steels fabricated by DED. Fig. 4 shows optical microscope images of the representative microstructures of the as-built AISI 316L stainless steel samples produced by using the fresh powder. A dendritic structure, free of macro defects is revealed, and the transition between the layers is easily detectable. In the cross-section of these samples, the borders of the following layers are clearly distinguishable. Since the building strategy consists of 0–90° alternated deposited layers, on each layer two different types of interface are present (Fig. 4(a)). Actually, on one layer curved borders of the melt pool are visible. The Gaussian distribution of laser energy induces this typical additive manufacturing microstructural feature. On the following deposited layer, flat borders are present. In this layer the melt pool is observed laterally. These different features of the laser tracks are generated by the alternated x/y raster laser scanning path.

The generation of a heat affected zone and melt pool during DED deposition, as well as the complex thermal regime induced by such process, is described elsewhere [24,25]. Solid conduction heat transfer mode dominates across the heat affected zone at melt pool border, whereas convective heat transfer mode dominates in the central zone of the melt pool, where liquid metal solidifies slightly later. Finally, a complex mix convective-conductive-radiating heat transfer occurs at the edges of the laser track, where the lateral borders of the melt pool are exposed to the operating environment. The observation of the microstructure within the first layer and the interface of deposited area/substrate (Fig. 4(b)) provides information on temperature gradients occurred within the melt pool itself during deposition. Along directions orthogonal to the curved melt pool borders temperature gradients are intense and clearly oriented. This results in a marked directional growth of the dendrites (i.e. mushy zone) from the melt pool borders and converging towards the centre of the melt pool. On the contrary, at such location, the heat transfer is not preferentially oriented and equiaxed dendrites more likely form.

As far as the whole section of the deposited component is concerned, the columnar structure growing in the direction the maximum thermal gradient dominated in the middle height of the sample (Fig. 4(c)), whereas in last deposited layer the cellular structure dominates (Fig. 4(d)). This is a consequence of the complex heat transfer occurring during the DED. Indeed, the microstructure of the first deposited layers (that entered in direct contact with the substrate) completely consists of an equiaxed microstructure, formed as a consequence of the homogeneous cooling rate occurring in these areas. As a matter of fact, the uniformly heated substrate acts as a heat sink and provides a uniform high cooling rate (G × R) that results in the formation of the equiaxed microstructure. Within the layers deposited later on this first basement of the sample, the role of the substrate becomes less effective since the conduction heat flow takes place through the previously deposited layer. These variations during sample building imply high G/R values with the consequent formation of the columnar microstructure.

In order to estimate the cooling rate occurred at different distances from the substrate and its total average value in both specimens, PCAS parameter was measured at four different distances by the method of the triangle. As mentioned before, at each specific distance from the substrate four images were acquired from the left to right side, and then on each image 10 measurements were implemented to include all the different PCAS sizes in the calculations. Therefore, through the consideration of various PCAS at each distance which is as result of different cooling rates from the edge to the centre of sample, the average cooling rate is calculated and reported for each specific distance from the substrate. Fig. 5(a and b) illustrates the SEM micrographs of DED AISI 316L samples fabricated with the fresh powder at various distances from the substrates. PCAS values of this sample as a function of the distance from the substrate are reported in Fig. 5(c). It is possible to note that by increasing the distance from the substrate from 2 to 14 mm, the PCAS values monotonously increase from 2.8 to 4.6 μm. Afterwards, close to the last layers, the level of PCAS suddenly drops to 3.3 μm.

According to literature, the major affecting factor on PCAS is the cooling rate during solidification [26,27], and the following equation is the most significant relationship between these two parameters:

$$\lambda_1 = 80\dot{T}^{-0.33} \quad (1)$$

Where λ_1 is PCAS and $\dot{T}$ is the cooling rate. To date, several studies have

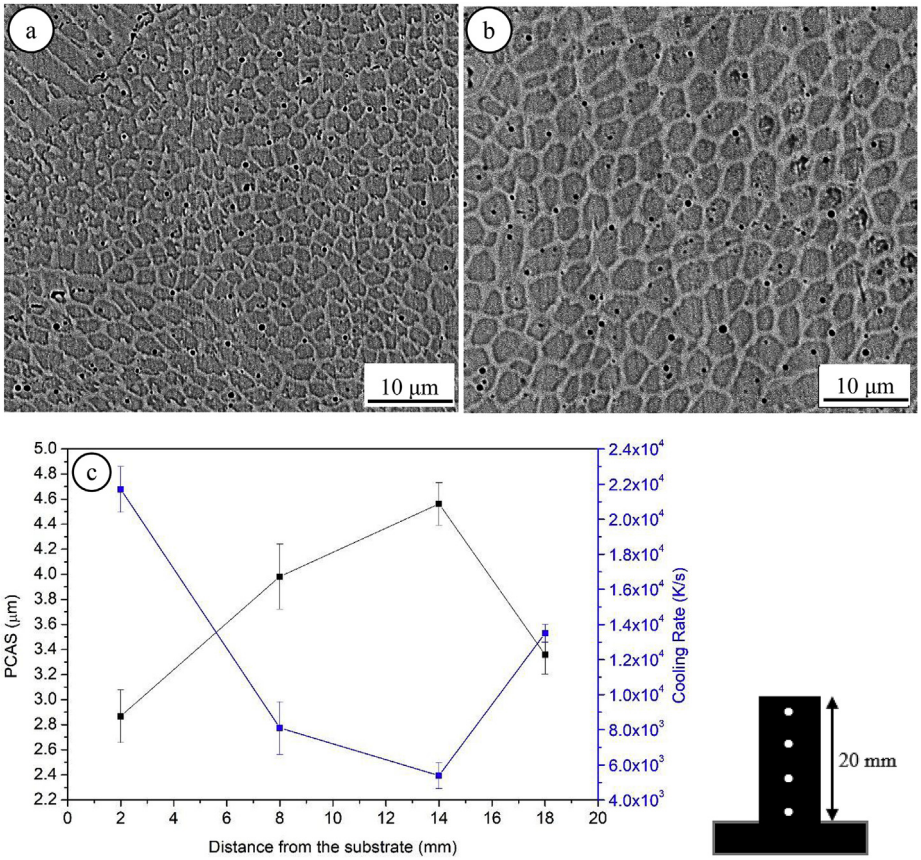


Fig. 5. SEM images of DED AISI 316L using fresh powder at: (a) 2 mm, (b) 14 mm from the deposition/substrate interface, (c) PCAS and cooling rate as a function of the distance from the substrate.

successfully used this equation to explain the relationship between the PCAS and the cooling rate for various austenitic stainless steels [2,28]. Thus, according to the aforementioned equation, the cooling rate at different distances from the substrate was calculated and plotted as a function of the distance from the substrate in Fig. 5(c). As it can be seen in this graph, by increasing the distance from the substrate the cooling rate decreases from 2.2×10^4 to 6×10^3 K/s and finally in the last layers it increases again to 1.4×10^4 K/s. These last deposited layers remain exposed to the operating environment in the absence of further deposited layer and can dissipate heat through the increased radiative surface (i.e. the top of the sample). This explains the anomalous increase of cooling rate in these layers and, consequently, the decreased PCAS recorded value with respect to the underlying layers.

According to the estimated cooling rates experienced by the different sections located at increasing distance from the substrate-sample interface, the average calculated cooling rate for all sample is 1.5×10^4 K/s and this value is in line with other literature works [2,29,30].

According to the above analysis, although with some local differences, the cooling rates applied from the deposition temperature to room temperature in the DED 316L are high. This key processing parameter drives the development of the microstructure of the samples in the as-built state. In a standard fast cooled austenitic stainless steel, depending on its chemical composition, two different microstructural constituents are obtained: austenite (γ) and, the so-called, δ-ferrite [31]. Since in DED process the cooling rate is always higher than those considered in traditionally fabricated steels and therefore the solidification is out of equilibrium condition, in addition to the conventional Schaeffler diagram (Fig. 6(a)) another diagram, based on Schaeffler and WRC-1992 predictive graphs is employed. This predictive phase diagram is named 'Pseudo-binary predictive' phase diagram (Fig. 6(b)) and applies only to austenitic stainless steels with a ferrite content between 0 to 100% [32]. It is worthwhile to note that the definitions of Cr- and Ni-equivalents are slightly different according to the standard Schaeffler diagram and to the WRC-1992 predictive methodology. In general, in 300 series of austenitic stainless steels the expected δ-ferrite content can be evaluated from the standard Schaeffler calculated equivalent contents of Cr and Ni (formulas are reported in x- and y-axis in Fig. 6(a)). This calculation was preliminarily applied to the AISI 316L powders (Table 2) in order to verify the theoretical gross content of δ-ferrite (red dot in Fig. 6(a)). Once the theoretical gross content of δ-ferrite was assessed to be between 5 and 10%, the WRC-1992 modified Cr- and Ni-equivalents formulas (formulas are reported in x- and y-axis in Fig. 6(a)) can be applied in order to locate our specific steel in the pseudo-binary phase diagram [33]. In the current work, in order to theoretically locate the current stainless steel with reference for to exist, the values of Cr_{eq} and Ni_{eq} are calculated according to equations by using the chemical composition of the starting powders (Table 2).

According to the WRC-1992 definitions of Cr- and Ni-equivalents the $Cr_{eq.}/Ni_{eq.}$ ratio was calculated to be 1.69. According to the pseudo-binary phase diagram, this value locates the 316L studied in the current work within the FA region, i.e. that of austenite + lathy ferrite (Fig. 7(a and b)). The ultimate formation of such microstructure can be explained as follows. During solidification, the primary δ-ferrite (δ_p) solidifies in the fusion zone. Within the L + δ field, the residual liquid remains enriched in γ-stabilizing elements, especially Ni and C, and thus solidifies in the γ structure. According to the WRC-1992 theory, the final microstructure for this specific $Cr_{eq.}/Ni_{eq.}$ ratio would be austenite + skeletal ferrite or austenite + lathy ferrite when moderate or fast cooling occur, respectively [31]. Independently by the local cooling rate occurring, a definite fraction of primary δ-ferrite is retained in the microstructure after cooling.

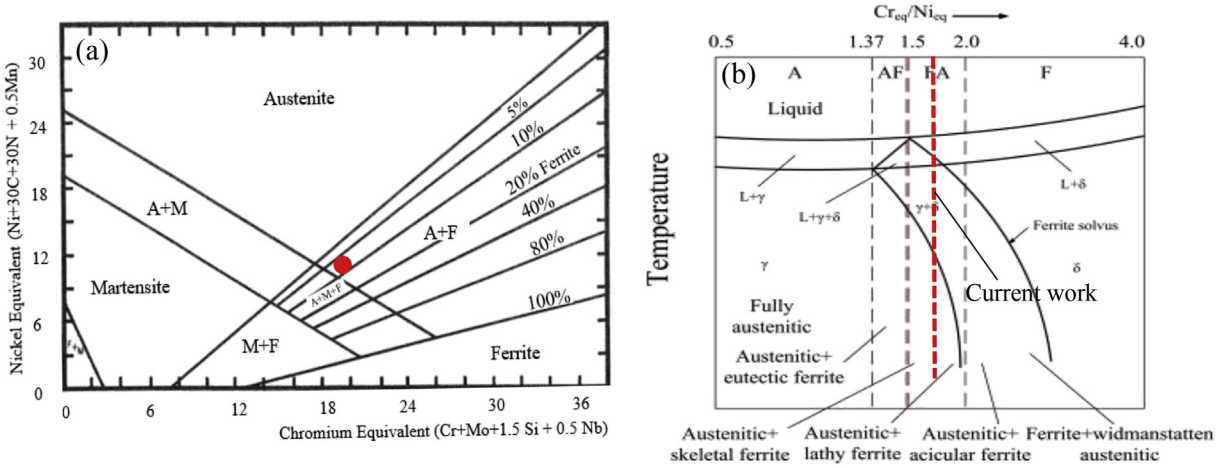


Fig. 6. (a) Schaeffler constitution diagram showing the location of the composition of the AISI 316L stainless steel powders, (b) Pseudo-binary phase diagram [32].

Table 2
The chemical composition of AISI 316L and its corresponding Cr and Ni equilibrium.

Composition	Wt.%
Carbon, C	0.017
Silicon, Si	0.46
Manganese, Mn	1.91
Chromium, Cr	17.20
Molybdenum, Mo	1.85
Nickel, Ni	10.20
Niobium, Nb	0.025
Chromium equivalent, $Cr_{eq.}$	19.75
Nickel equivalent, $Ni_{eq.}$	11.66

When one tries to apply these theoretical assumptions to the microstructure features provided by the DED process of AISI 316L one has to consider that reference $Cr_{eq.}/Ni_{eq.}$ ratios in the Pseudo-binary phase diagram were determined under conditions of near equilibrium that are far away from those of any additive process. Actually, in this case, it is worthwhile to consider the role both of fast directional solidification [34] and of re-heating occurring in the HAZ [35] due to the further layer depositions. Both these aspects promote intense partitioning of alloying elements, which locally generate microsegregation of γ- and δ-stabilizers. These effects lead to local variations of the $Cr_{eq.}/Ni_{eq.}$ ratio, thus making the exact prevision of the different microstructural features, is very difficult. The partitioning coefficients of the different alloying elements in these conditions are rather difficult to be accurately determined, however there is a general agreement in the literature [34–36] that in AISI 316L welds or laser surface treated AISI 316L, the last fraction of liquid that solidifies enriches in δ-stabilizers, especially Mo, Si and Cr. According to this, the interdendritic regions can be expected to represent sites for preferential δ-ferrite formation.

Actually, FESEM micrographs/EDS analysis (Fig. 7(a and b)) of the samples fabricated for this study, confirmed the formation of a duplex

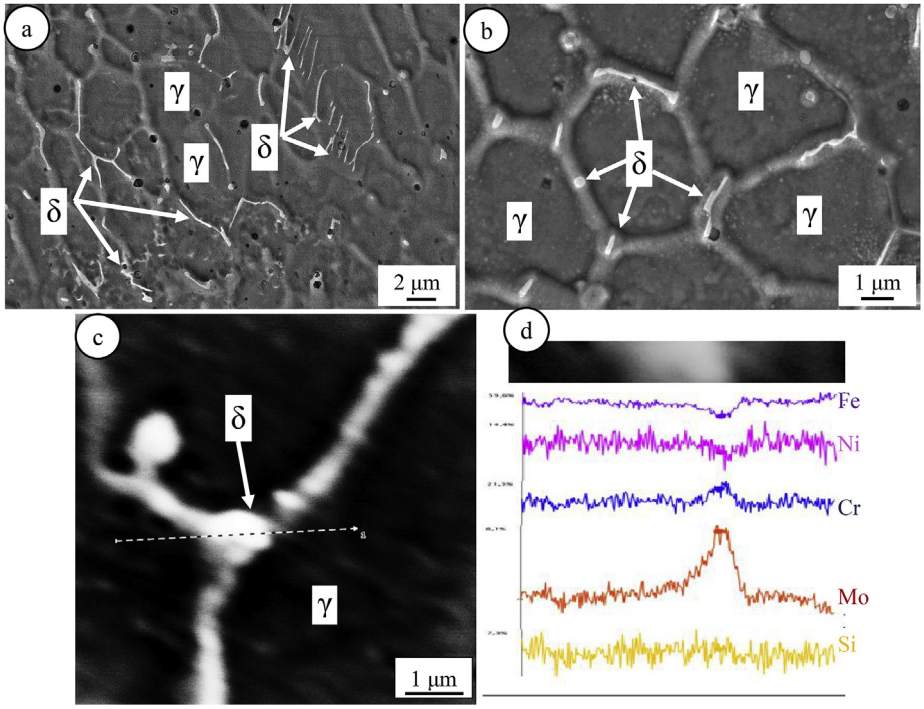


Fig. 7. (a–b) FESEM images of AISI 316 fabricated by DED confirming the presence of residual delta ferrite, (c–d) EDS line profile on a dendritic arm confirming the presence of delta ferrite in the microstructure.

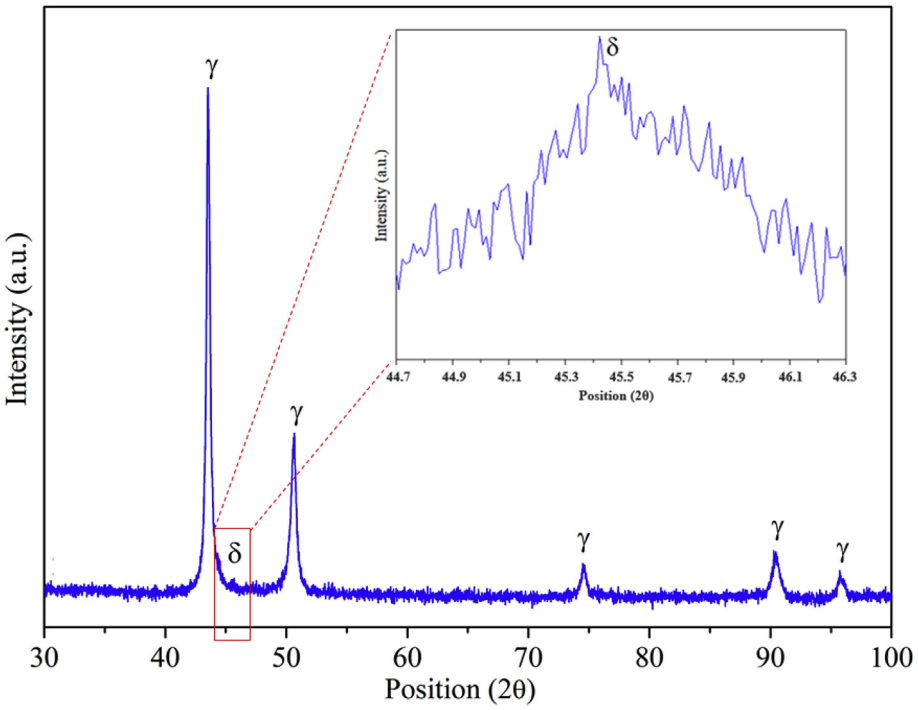


Fig. 8. X-ray diffraction pattern of as-built AISI 316L sample.

microstructure during DED of AISI 316L samples. In particular, Fig. 7(c) and (d), showing the location and related results of EDS line analysis across an interdendritic arm, confirms the enrichment in δ-stabilizer elements, especially Mo and Cr, at these sites. As discussed earlier, this result demonstrates that at high cooling rates, as those involved in DED process, the solidifying austenite consumes austenite-promoting elements like nickel, carbon, and nitrogen and accordingly, enriches the residual liquid fractions in ferrite stabilizers, thus leading to the possibility to form ferrite at some interdendritic regions. Furthermore, the presence of a small peak at the angle of 44.7° in the XRD pattern of these sample suggest the presence of residual δ-ferrite in the final microstructure (Fig. 8).

Apart from the presence of residual δ-ferrite, it is also found that there is a correlation between the percentage of residual δ-ferrite and cooling rate at different distance from the substrate. In fact, it is revealed that by increasing the distance from the substrate up to 14 mm, as a consequence of decreasing the cooling rate and increasing the number of re-heating, the residual δ-ferrite content decreases from 4.8% to 1.3%. Thereafter, at the last layers due to the increment of cooling rate the percentage of residual δ-ferrite increases markedly up to 4.2%.

The overall microstructure features described above on samples manufactured starting from fresh powder were also found in samples manufactured starting from recycled powders. However, as it can be seen in Fig. 9, the sample produced by recycled powder additionally contains some spherical inclusions (2.4%). According to the EDS line analysis performed on the polished surface of samples produced by recycled powders, the composition of the revealed inclusions is a mix of Mn/Si-oxides. These mixed oxide structures are typical re-oxidation product found during ladle practice of highly containing Mn/Si steels [37–39]. Due to the affinity of such elements to oxygen, the formation of re-oxidation product is hardly avoidable even in the secondary steelmaking process, which is nowadays very robust manufacturing process. Therefore, it is not surprising that, although shield gas flow was used to reduce the amount of oxygen entering in contact with the liquid steel pool, such non-metallic inclusions were formed during DED deposition. Since no thermomechanical processing is applied in this case (contrary to traditional steelmaking) these non-metallic particles maintain a spherical shape, which is less detrimental to mechanical properties. Nevertheless, the frequency and average dimension of these inclusions (≈12 μm) can markedly influence the ultimate 316L properties, especially the ductility.

3.2. Mechanical properties

To evaluate the effect of the type of powders on the mechanical performance of AISI 316L alloy, tensile tests were performed on samples produced using fresh and recycled powders (Fig. 10).

As can be seen in Fig. 10, AISI 316L samples produced using fresh and recycled powders exhibit many differences in the stress-strain curve shape. Although the work hardening behaviour is practically the same for all samples, the most evident difference is that related to elongation to fracture, that for samples produced with fresh powders is more than 50% higher than that of samples produced with recycled ones. Additionally, all samples produced with recycled powders exhibit a sudden drop in the stress-strain curve just after reaching the ultimate tensile strength, with limited strain accumulated within the region of the geometrical instability, i.e. when transversal strain occurs. Both these aspects can be addressed to the presence of coarse Mn/Si oxides in these samples, as discussed in the previous section. The frequent presence of isolated coarse particles (i.e. 7–15 μm) and, even more, of clusters of these particles generate embrittlement effect that drastically reduces the maximum capacity of plastically deform of the AISI 316L matrix. On the other hand, these oxide particles would provide a sort of dispersion strengthening effect, with a consequent improvement in mechanical levels [40,41]. Nevertheless, in the current study, such effect was observed only in a few samples, actually exhibiting markedly higher YS and UTS levels. The scattering of mechanical levels in samples fabricated with recycled powders can be ascribed to the fact that, although oxide particles are always introduced in the AISI 316L matrix, their dispersion is definitively not uniform as a consequence of a not controlled dispersion strengthening process. The same reason can explain the fact that only one of these samples has slightly lower YS a UTS and higher elongation to fracture (ca. 5% in excess) with respect to

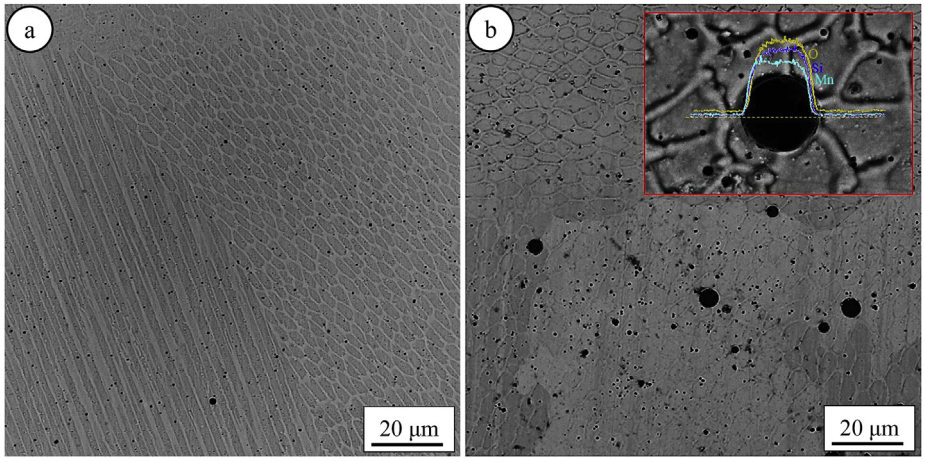


Fig. 9. SEM microstructure of DED AISI 316L using (a) fresh, and (b) recycled powder.

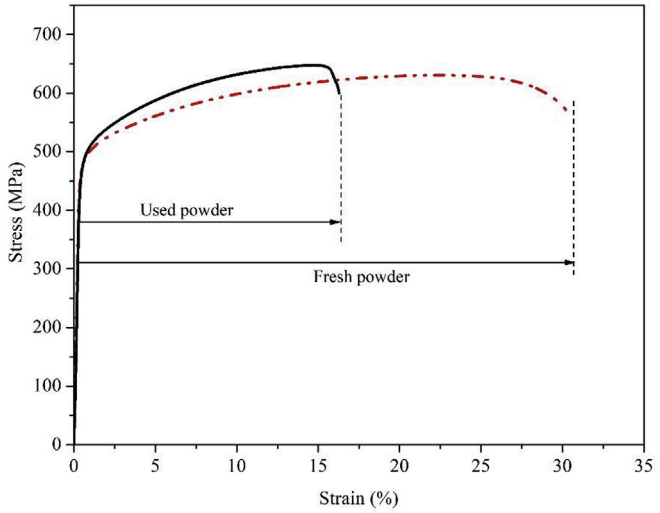


Fig. 10. Stress-strain curves of AISI 316L produced by DED using fresh and recycled powders.

other similar samples. A certain scattering in the elongation to fracture was also recorded for samples fabricated with fresh powders (data has scattering band of ca. 8%). As discussed earlier, although the Mn/Si oxides average size is much lower (i.e. sub-micrometric), also samples fabricated with fresh powders exhibit a dispersion of these oxides within the matrix. This can result in a fluctuation of the elongation to fracture data because of different dispersion efficiency of such oxides.

The comparison of the fracture surfaces built with fresh and recycled powders (Fig. 11) revealed the presence of large oxide particles in samples fabricated with recycled powders (brittle phases indicated by the red arrows in Fig. 11(b)). The size and distribution of these embrittling phases strongly affect the mechanical behaviour of these samples.

Apart from the influence of oxides, the matrix-fracture surfaces in all tensile samples (both fabricated with fresh and recycled powders, Fig. 11(a) and (b)) are typical ductile fracture with fine dimples structure. The dimples extension observed on the fracture surfaces of all the specimens was limited to the size of the cellular dendritic structure obtained by DED fabrication. Actually, it is found that dimples size is comparable to the fine PCAS (e.g. see Fig. 6). This means that plastic deformation is somehow limited within the borders of cellular dendritic structure. Whereas, in samples fabricated with recycled powders, bigger dimples are present around coarse oxides, which appear fractured as a consequence of the fracture propagation. According to EDS map analysis carried out on the fracture surface of samples produced by recycled powders (Fig. 12), the composition of the revealed inclusions is compatible with that of the inclusions in the starting microstructure. This confirms that dispersed oxides partially contribute to strengthening the DED AISI 316L matrix, but especially to limit the maximum elongation achievable.

The mechanical levels of AISI 316L produced in this work via DED using fresh powders are comparable (see Table 3) with literature data for DED and selective laser melting (SLM). The higher mechanical strength of AM samples in comparison with samples produced by the conventional methods, such as casting and forging, is attributed to the finer microstructure formed as a consequence of fast cooling during these manufacturing routes [42]. Moreover, the presence of δ-ferrite phase dispersed along interdendritic regions of AISI 316L after rapid solidification processes is supposed to strengthen the soft austenitic matrix and consequently to reduce its ductility [43]. However, according to the fracture surface of samples, the failure of specimens started from the interface of matrix and inclusions, and thus it can be concluded that the presence of oxides in these samples plays the most detrimental role in the ductility of AISI 316L produced by DED.

4. Conclusions

In this work, a comprehensive study on the cooling rate, primary cellular arm spacing, microstructure and mechanical properties of AISI 316L stainless steel produced via DED is reported. The effect of powder recycling on the microstructure and mechanical properties of AISI 316L specimens is also addressed in order to compare the properties achieved using recycled powders and those achieved using fresh powders, as well as with literature data. The main conclusions can be drawn as follow:

1. The columnar structure growing in the direction of the maximum thermal gradient dominated at the middle height of the sample, whereas in last deposited layers the cellular structure dominates.
2. By increasing the distance from the substrate, the PCAS values monotonously increases. However, within the last deposited layers, suddenly the level of PCAS drops because of the changes occurred in the cooling mechanisms at such location. This is strictly related to cooling rate that, by increasing the deposition height, decreases from 2.2×10^4 to 6×10^3 K/s and finally in the last deposited layers, due to the marked contribution of radiation in the cooling, it increases again to 1.4×10^4 K/s.
3. AISI 316L samples produced using fresh and recycled powders behave drastically different, especially in terms of elongation, that reduces by more than 50% when recycled powder is used for samples fabrication.

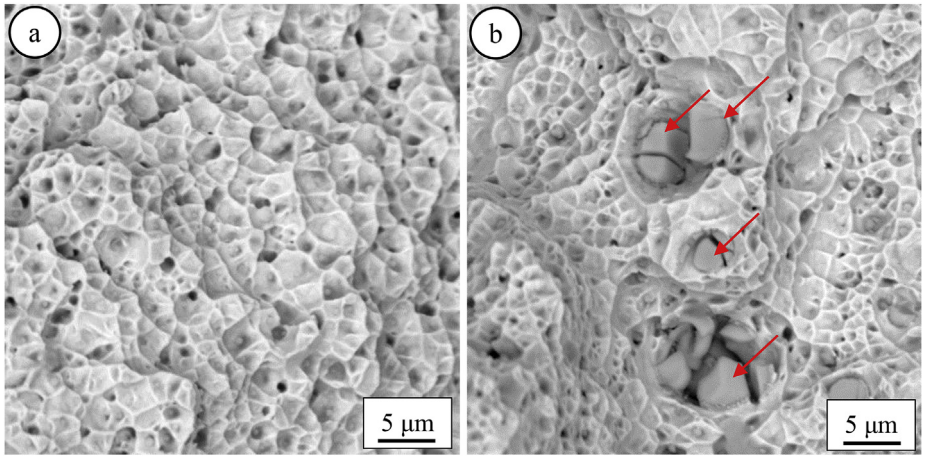


Fig. 11. Typical tensile test fracture morphologies of AISI 316L stainless steel samples produced by DED using (a) fresh powder, (b) recycled powder.

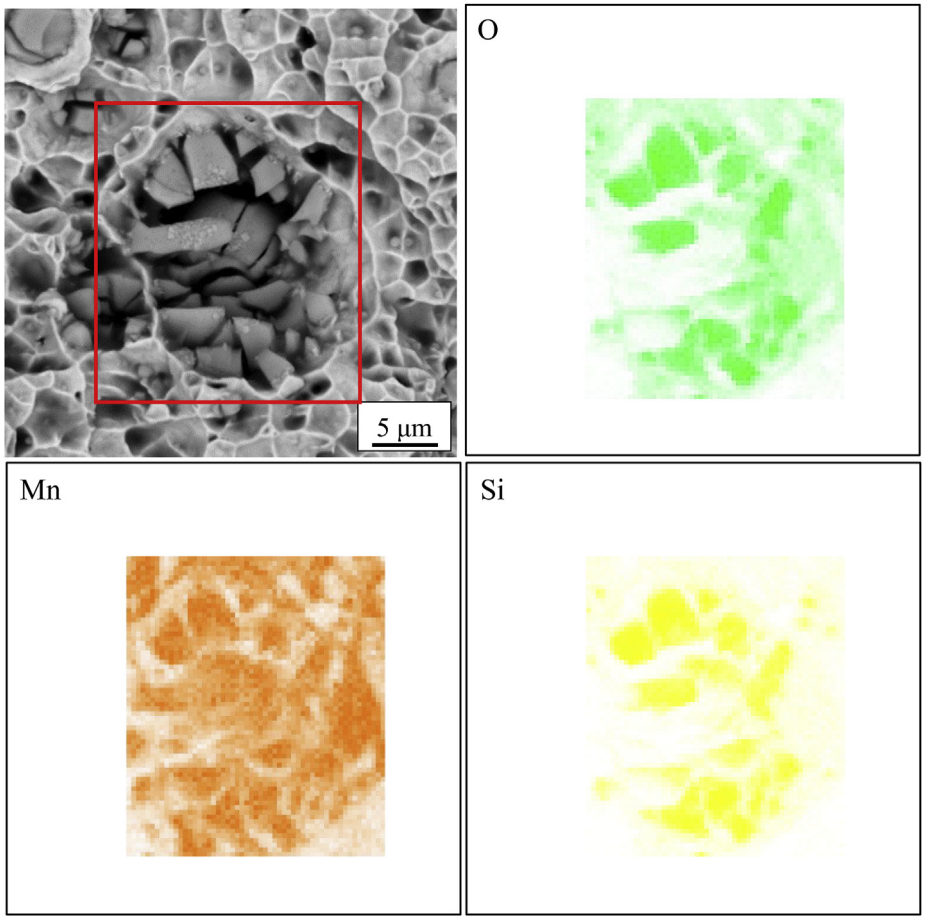


Fig. 12. SEM-EDS mapping of inclusions in the as-deposited AISI 316L stainless steel fracture surfaces of a sample built with recycled powder.

Table 3
Tensile properties of the AISI 316L samples produced by the different production process.

	Powder	E (GPa)	YS (MPa)	UTS (MPa)	ε_r (%)	Ref.
DED	Fresh	177.2 ± 6.9	469.6 ± 3.4	628.2 ± 6.6	31.2 ± 2.2	Current work
DED	Used	200.3 ± 3.3	458.4 ± 29.9	651.6 ± 43.9	16.2 ± 2.1	Current work
DED			405–415	620–660	32–40	[2]
SLM			495–500	610–620	38–48	[44]
As Cast			262	552	55	[45]
Wrought			255–310	450	30	[42]

4. The large variation in the strain-to-fracture observed in the two different sets of samples produced by recycled and fresh powder is attributed to the presence of large inclusions like oxides rich in Mn and Si with 7–15 μm in diameter. Such inclusions are observed also in samples produced using fresh powders, but their frequency and size is incredibly lower.
5. The higher mechanical strength of DED samples in comparison with the samples produced by the conventional methods such as casting and forging is attributed to the finer microstructure and final phase composition of DED samples that forms as a consequence of fast cooling during the production (10^3–10^4 K/s).

Acknowledgements

The authors would like to acknowledge the European research project belonging to the Horizon 2020 Research and Innovation Programme; Borealis—the 3A energy class Flexible Machine for the new Additive and Subtractive Manufacturing on next generation of complex 3D metal parts (Grant agreement no.: 633992).

Appendix A. Supplementary data

Supplementary data to this article can be found online at https://doi.org/10.1016/j.msea.2019.138360. Fig. Supplementary 1

References

[1] M.S.F. de Lima, S. Sankaré, Microstructure and mechanical behavior of laser additive manufactured AISI 316 stainless steel stringers, Mater. Des. 55 (2014) 526–532 https://doi.org/10.1016/j.matdes.2013.10.016.
[2] M. Ma, Z. Wang, X. Zeng, A comparison on metallurgical behaviors of 316L stainless steel by selective laser melting and laser cladding deposition, Mater. Sci. Eng. A 685 (2017) 265–273 https://doi.org/10.1016/j.msea.2016.12.112.
[3] A. Saboori, D. Gallo, S. Biamino, P. Fino, M. Lombardi, An overview of additive manufacturing of titanium components by directed energy deposition: microstructure and mechanical properties, Appl. Sci. 7 (2017), https://doi.org/10.3390/app7090883.
[4] X. Xu, G. Mi, Y. Luo, P. Jiang, X. Shao, C. Wang, Morphologies, microstructures, and mechanical properties of samples produced using laser metal deposition with 316L stainless steel wire, Opt. Lasers Eng. 94 (2017) 1–11 https://doi.org/10.1016/j.optlaseng.2017.02.008.
[5] A. Saboori, A. Aversa, G. Marchese, S. Biamino, M. Lombardi, P. Fino, Application of directed energy deposition-based additive manufacturing in repair, Appl. Sci. 9 (2019), https://doi.org/10.3390/app9163316.
[6] I. Gibson, D. Rosen, B. Stucker, Directed energy deposition processes, Addit. Manuf. Technol. 3D Printing, Rapid Prototyping, Direct Digit. Manuf, Springer, New York, New York, NY, 2015, pp. 245–268, , https://doi.org/10.1007/978-1-4939-2113-3_10.
[7] A. Saboori, S. Biamino, M. Lombardi, S. Tusacciu, M. Busatto, M. Lai, P. Fino, How the nozzle position affects the geometry of the melt pool in directed energy deposition process, Powder Metall. 62 (2019) 213–217, https://doi.org/10.1080/00325899.2019.1627490.
[8] S.A. Khairallah, A.T. Anderson, A. Rubenchik, W.E. King, Laser powder-bed fusion additive manufacturing: physics of complex melt flow and formation mechanisms of pores, spatter, and denudation zones, Acta Mater. 108 (2016) 36–45 https://doi.org/10.1016/j.actamat.2016.02.014.
[9] J. Mazumder, J. Choi, K. Nagarathnam, J. Koch, D. Hetzner, The direct metal deposition of H13 tool steel for 3-D components, JOM 49 (1997) 55–60, https://doi.org/10.1007/BF02914687.
[10] M. JD, A. Pinkerton, Z. Liu, I. Manna, L. Li, Microstructure characterisation and process optimization of laser assisted rapid fabrication of 316L stainless steel, Appl. Surf. Sci. 247 (2005) 320–327, https://doi.org/10.1016/j.apsusc.2005.01.039.
[11] P. Ganesh, R. Giri, R. Kaul, P. Ram Sankar, P. Tiwari, A. Atulkar, R.K. Porwal, R.K. Dayal, L.M. Kukreja, Studies on pitting corrosion and sensitization in laser rapid manufactured specimens of type 316L stainless steel, Mater. Des. 39 (2012) 509–521, https://doi.org/10.1016/j.matdes.2012.03.011.
[12] K. Zhang, S. Wang, W. Liu, X. Shang, Characterization of stainless steel parts by laser metal deposition shaping, Mater. Des. 55 (2014) 104–119 https://doi.org/10.1016/j.matdes.2013.09.006.
[13] J.D. Majumdar, A. Pinkerton, Z. Liu, I. Manna, L. Li, Mechanical and electrochemical properties of multiple-layer diode laser cladding of 316L stainless steel, Appl. Surf. Sci. 247 (2005) 373–377 https://doi.org/10.1016/j.apsusc.2005.01.131.
[14] X. Wang, D. Deng, M. Qi, H. Zhang, Influences of deposition strategies and oblique angle on properties of AISI316L stainless steel oblique thin-walled part by direct laser fabrication, Opt. Laser. Technol. 80 (2016) 138–144 https://doi.org/10.1016/j.optlastec.2016.01.002.
[15] Z. Wang, T.A. Palmer, A.M. Beese, Effect of processing parameters on microstructure and tensile properties of austenitic stainless steel 304L made by directed energy deposition additive manufacturing, Acta Mater. 110 (2016) 226–235 https://doi.org/10.1016/j.actamat.2016.03.019.
[16] M. Ziętala, T. Durejko, M. Polański, I. Kunce, T. Płociński, W. Zieliński, M. Łazińska, W. Stępniowski, T. Czujko, K.J. Kurzydłowski, Z. Bojar, The microstructure, mechanical properties and corrosion resistance of 316L stainless steel fabricated using laser engineered net shaping, Mater. Sci. Eng. A 677 (2016) 1–10 https://doi.org/10.1016/j.msea.2016.09.028.
[17] A. Yadollahi, D. Seely, B. Patton, N. Shamsaei, Microstructural features and mechanical properties of 316L stainless steel fabricated by laser additive manufacture, 56th AIAA/ASCE/AHS/ASC Struct. Struct. Dyn. Mater. Conf, American Institute of Aeronautics and Astronautics, 2015, , https://doi.org/10.2514/6.2015-1355.
[18] J. Li, D. Deng, X. Hou, X. Wang, G. Ma, D. Wu, G. Zhang, Microstructure and performance optimisation of stainless steel formed by laser additive manufacturing, Mater. Sci. Technol. 32 (2016) 1223–1230, https://doi.org/10.1080/02670836.2015.1114774.
[19] X. Wang, D. Deng, H. Yi, H. Xu, S. Yang, H. Zhang, Influences of pulse laser parameters on properties of AISI316L stainless steel thin-walled part by laser material deposition, Opt. Laser. Technol. 92 (2017) 5–14, https://doi.org/10.1016/j.optlastec.2016.12.021.
[20] F. Bosio, A. Saboori, A. Lacagnina, E. Librera, M. De Chirico, S. Biamino, P. Fino, M. Lombardi, Directed energy deposition of 316L steel: effect of type of powders and gas related parameters, Euro PM2018 Congr, Exhebition, Bilbao (Spain), 2018, pp. 1–6.
[21] A. Saboori, F. Bosio, E. Librera, M. De Chirico, S. Biamino, M. Lombardi, P. Fino, Accelerated process parameter optimization for directed energy deposition of 316L stainless steel, Euro PM2018 Congr, Exhebition, Bilbao (Spain), 2018, pp. 1–6.
[22] A. Saboori, D. Gallo, S. Biamino, P. Fino, M. Lombardi, An overview of additive manufacturing of titanium components by directed energy deposition: microstructure and mechanical properties, Appl. Sci. (2017), https://doi.org/10.3390/app7090883.
[23] C. Selcuk, Laser metal deposition for powder metallurgy parts, Powder Met 54 (2011) 94–99.
[24] W. Li, M. Soshi, Modeling analysis of grain morphologies in Directed energy deposition (DED) coating with different laser scanning patterns, Mater. Lett. 251 (2019) 8–12 https://doi.org/10.1016/j.matlet.2019.05.027.
[25] B. De La Batut, O. Fergani, V. Brotan, M. Bambach, M. El Mansouri, Analytical and numerical temperature prediction in direct metal deposition of Ti6Al4V, J. Manuf. Mater. Process. 1 (2017), https://doi.org/10.3390/jmmp1010003.
[26] H.S. Kim, Y. Kobayashi, S. Tsukamoto, K. Nagai, Effect of cooling rate on microstructure evolution of rapidly cooled high-impurity steels, Mater. Sci. Eng. A 403 (2005) 311–317 https://doi.org/10.1016/j.msea.2005.05.049.
[27] H. Yin, S.D. Felicelli, Dendrite growth simulation during solidification in the LENS process, Acta Mater. 58 (2010) 1455–1465 https://doi.org/10.1016/j.actamat.2009.10.053.
[28] J.W. Fu, Y.S. Yang, J.J. Guo, W.H. Tong, Effect of cooling rate on solidification microstructures in AISI 304 stainless steel, Mater. Sci. Technol. 24 (2008) 941–944, https://doi.org/10.1179/174328408X295962.
[29] M.H. Farshidianfar, A. Khajepour, A.P. Gerlich, Effect of real-time cooling rate on microstructure in Laser Additive Manufacturing, J. Mater. Process. Technol. 231 (2016) 468–478 https://doi.org/10.1016/j.jmatprotec.2016.01.017.
[30] S. Gorsse, C. Hutchinson, M. Gouné, R. Banerjee, Additive manufacturing of metals: a brief review of the characteristic microstructures and properties of steels, Ti-6Al-4V and high-entropy alloys, Sci. Technol. Adv. Mater. 18 (2017) 584–610, https://doi.org/10.1080/14686996.2017.1361305.
[31] B. Kocabekir, R. Kaçar, S. Gündüz, F. Hayat, An effect of heat input, weld atmosphere and weld cooling conditions on the resistance spot weldability of 316L austenitic stainless steel, J. Mater. Process. Technol. 195 (2008) 327–335 https://doi.org/10.1016/j.jmatprotec.2007.05.026.
[32] P. Guo, B. Zou, C. Huang, H. Gao, Study on microstructure, mechanical properties and machinability of efficiently additive manufactured AISI 316L stainless steel by high-power direct laser deposition, J. Mater. Process. Technol. 240 (2017) 12–22 https://doi.org/10.1016/j.jmatprotec.2016.09.005.
[33] M. Dadfar, M.H. Fathi, F. Karimzadeh, M.R. Dadfar, A. Saatchi, Effect of TIG welding on corrosion behavior of 316L stainless steel, Mater. Lett. 61 (2007) 2343–2346 https://doi.org/10.1016/j.matlet.2006.09.008.
[34] P.L. Ferrandini, C.T. Rios, A.T. Dutra, M.A. Jaime, P.R. Mei, R. Caram, Solute segregation and microstructure of directionally solidified austenitic stainless steel, Mater. Sci. Eng. A (2006) 435–436 139–144 https://doi.org/10.1016/j.msea.2006.07.024.
[35] S. Atamert, J.E. King, Elemental partitioning and microstructural development in duplex stainless steel weld metal, Acta Metall. Mater. 39 (1991) 273–285 https://doi.org/10.1016/0956-7151(91)90306-L.
[36] Z. Zhang, H. Jing, L. Xu, Y. Han, L. Zhao, J. Zhang, Influence of microstructure and elemental partitioning on pitting corrosion resistance of duplex stainless steel welding joints, Appl. Surf. Sci. 394 (2017) 297–314 https://doi.org/10.1016/j.apsusc.2016.10.047.
[37] F. Yan, W. Xiong, E. Faierson, G.B. Olson, Characterization of nano-scale oxides in austenitic stainless steel processed by powder bed fusion, Scr. Mater. 155 (2018) 104–108 https://doi.org/10.1016/j.scriptamat.2018.06.011.
[38] A.O. Kluken, Ø. Grong, Mechanisms of inclusion formation in Al − Ti − Si − Mn deoxidized steel weld metals, Metall. Trans. A. 20 (1989) 1335–1349, https://doi.org/10.1007/BF02665492.
[39] S.S. Babu, S.A. David, J.M. Vitek, K. Mundra, T. DebRoy, Development of macro- and microstructures of carbon–manganese low alloy steel welds: inclusion

formation, Mater. Sci. Technol. 11 (1995) 186–199, https://doi.org/10.1179/mst.1995.11.2.186.
[40] A. Saboori, R. Casati, A. Zanatta, M. Pavese, C. Badini, M. Vedani, Effect of graphene nanoplatelets on microstructure and mechanical properties of alsi10mg nanocomposites produced by hot extrusion, Powder Metall. Met. Ceram. 56 (2018) 647–655.
[41] A. Saboori, S.K. Moheimani, M. Dadkhah, M. Pavese, C. Badini, P. Fino, An overview of key challenges in the fabrication of metal matrix nanocomposites reinforced by graphene nanoplatelets, Metals (Basel) 8 (2018) 172, https://doi.org/10.3390/met8030172.
[42] A. Yadollahi, N. Shamsaei, S.M. Thompson, D.W. Seely, Effects of process time interval and heat treatment on the mechanical and microstructural properties of direct laser deposited 316L stainless steel, Mater. Sci. Eng. A 644 (2015) 171–183 https://doi.org/10.1016/j.msea.2015.07.056.
[43] Z. Sun, X. Tan, S.B. Tor, W.Y. Yeong, Selective laser melting of stainless steel 316L with low porosity and high build rates, Mater. Des. 104 (2016) 197–204 https://doi.org/10.1016/j.matdes.2016.05.035.
[44] R. Casati, J. Lemke, M. Vedani, Microstructure and fracture behavior of 316L austenitic stainless steel produced by selective laser melting, J. Mater. Sci. Technol. 32 (2016) 738–744 https://doi.org/10.1016/j.jmst.2016.06.016.
[45] T. Kurzynowski, K. Gruber, W. Stopyra, B. Kuźnicka, E. Chlebus, Correlation between process parameters, microstructure and properties of 316 L stainless steel processed by selective laser melting, Mater. Sci. Eng. A 718 (2018) 64–73 https://doi.org/10.1016/j.msea.2018.01.103.